Arabian Journal of Chemistry (2021) **14**, 103325

King Saud University

Arabian Journal of Chemistry

www.ksu.edu.sa
www.sciencedirect.com

ORIGINAL ARTICLE

Theoretical study for determining the type of interactions between a GG block of an alginate chain with metals Cu^{2+}, Mn^{2+}, Ca^{2+} and Mg^{2+}

Carlos Soloaga Ardiles *, **Cristian Castro Rodríguez**

Departamento de Química, Facultad de Ciencias, Universidad de Tarapacá, Avenida General Velásquez 1775, Casilla 7D, Arica, Chile

Received 28 April 2021; revised 5 July 2021; accepted 6 July 2021
Available online 15 July 2021

KEYWORDS

Alginate;
Alginate affinity;
Alginate metal interaction

Abstract The alginate interaction with divalent cations has been the subject of extensive study since this biopolymer forms hydrogels in the presence of divalent cations (ionic crosslinking), which exhibit important properties with applications in fields such as medicine. It has been proposed that the properties of the hydrogel formed from the ionic crosslinking process depend, among several factors, on the type of interactions between the polymer and divalent metals. In this work, theoretical calculations based on density functional theory (DFT) were used to determine the chemical stability and the type of interaction between alginate and Cu^{2+}, Mn^{2+}, Ca^{2+} and Mg^{2+} cations. For this, the lowest energy geometries were determined at the B3LYP 6-31G (d, p) level of theory for the systems formed with Ca^{2+} and Mg^{2+}, while those formed with Cu^{2+} and Mn^{2+} used effective central potential (ECP) with LanL2DZ bases. The following models were used to characterize the bonds between the oxygen atoms of the polymer chain with the different metals; theory of non-covalent interactions (NCI), natural bonding orbitals (NBO) method, and topological analysis of the electronic location function (ELF). Our results showed that the properties such as chemical stability of the systems would be correlated with the degree of covalence of the bonds and the delocalization phenomena charge, where the systems constituted with Cu^{2+} and Mn^{2+} formed bonds with highly polarized covalent characteristics, while Ca^{2+} and Mg^{2+} form bonds of the electrostatic type. Nevertheless, our results support the idea proposed by previous studies; regarding the lack of correlation between the alginate for divalent cations affinity with the strength of the interactions between these metals and the polymer.

* Corresponding author.
E-mail addresses: delgaradh@gmail.com, csoloaga@academicos.uta.cl (C.S. Ardiles).

Peer review under responsibility of King Saud University.

ELSEVIER Production and hosting by Elsevier

1. Introduction

Alginate hydrogels, friendly to the environment, are very popular due to their wide use in the food industry, cosmetics, pharmacy, and others (Hasan et al., 2020a, 2020b, 2020c). Alginate is a biopolymer widely researched for the removal of metals from dilute aqueous solutions. One of its known applications is the adsorption of different metal ions

https://doi.org/10.1016/j.arabjc.2021.103325
1878-5352

such as Cu^{2+}, Mn^{2+}, Ca^{2+} and Mg^{2+}, which may be present in aqueous tributaries (Chen et al., 2020). Another important application of this biopolymer is its stabilizing capacity for nanoparticles, used in the degradation of certain pollutant (Hasan et al., 2020a, 2020b, 2020c). However, they also attract particular interest in modern biomedicine and regenerative medicine for applications in drug delivery systems and tissue engineering (Henkel et al., 2013). Bone is the most frequently transplanted tissue, together with cartilage. These, followed by skin, have focused on scientific efforts to achieve their regeneration; however, the results have not been optimal (Bouhadir et al., 2000). Among the different materials used for this purpose, the use of biomaterials with high water content, such as alginate hydrogels, represents an interesting proposal. However, the main disadvantage is their complex degradation and the use of high molecular weight alginates to obtain mechanical properties similar to those of hard tissues (Xu and Lam, 2018). One of the methods aimed at improving the properties of hydrogels is ionic crosslinking. This method combines alginates with divalent cations (Bidarra et al., 2014). Alginates present different affinities towards different divalent ions, giving rise to gels with different stability, permeability and strength, depending on the metal (Mørch et al., 2012). Based on such studies, the following order of alginate affinity to different divalent ions has been established: Pb > Cu > Cd > Ba > Ba > Sr > Sr > Ca > Co Ni, Zn, Mn > Mg, which would determine the physical properties of ionically crosslinked alginate gels (Haug, 1961).

Alginate is the generic term used to refer to salts and derivatives of alginic acid. This polysaccharide occurs as a mixture of insoluble salts, mostly sodium and potassium in brown algae (Phaeophyceae). Alginic acid is a high molecular weight polysaccharide consisting of different proportions of D-mannuronic acid and L-guluronic acid. The variation in the proportions of both acids depends mainly on the species of algae used (Hasan, 2020). The algae synthesize the alginate initially as a polymer of mannuronic acid, which they subsequently modified by transforming units of mannuronic acid into guluronic acid through an enzymatic epimerization. The final product contains zones formed by mannuronic acid another formed by guluronic acid, and other zones formed by both alternating acids (Wang et al., 2019). The zones of mannuronic acid are almost flat, with a structure similar to a belt, while those of guluronic acid have a structure with recesses and protrusions, as shown in Fig. 1.

The divalent cations interact mostly with monomer G blocks, which would be determinant in the properties of the hydrogel, where the bonds would be with the carboxyl groups ($–COO^-$) and hydroxyl groups (–OH) (Li et al., 2007). The mechanism consists of divalent ions with four carboxyl groups to form the egg crate model (Grant et al., 1973). This coordinating would influence the hydrogel's properties; for example, Zn^{2+} cations interact with alginate at different sites concerning Ca^{2+} ions, being less selective, which generates a more extensive crosslinking (Chan et al., 2002). On the other hand, attempts have been made to determine the ionic character of the metal–oxygen bonds in the formation of metal-alginate complexes, correlating the change of the asymmetric vibration of the carboxylic group ($–COO^-$), concerning a reference element, which would allow determining the ionic percentage of the bond (PIB) (Filipiuk et al., 2005). Other authors, however, mention that this method may present erroneous results due to an erroneous assignment of the ν (COO^-) peak by FTIR infrared spectroscopy (Papageorgiou et al., 2010).

However, results have been reported based on theoretical calculations of interaction energy, where it is concluded that metal–oxygen bonds with transition metals would be of the covalent type and electrostatic interactions for alkali earth elements (Agulhon et al., 2012). Both studies suggest that the affinity of alginate for different divalent cations would not correlate with the metal-polymer bond's strength. From these considerations, our main objective is to deepen the chemical nature of the interaction between alginate polymer with different divalent metals to provide information that contributes to the improvement in the methods of obtaining alginate hydrogels. In the present study, the problem is approached from a theoretical perspective, using the methods proposed by the density functional theory (DFT), non-covalent interaction (NCI) theory, natural orbital analysis (NBO), and electronic location function (ELF) analysis. For our purposes, the model used considers that the main interactions would occur with the oxygens of the functional groups derived from carboxylic acids and hydroxyl groups present in the polymer's G-blocks (Kohn, 1975). The model consists of a chain composed of two MM blocks linked to two GG blocks, which were made to interact with the following divalent metal ions; Cu^{2+}, Mn^{2+}, Ca^{2+} and Mg^{2+}. The choice of these elements is since Cu^{2+} and Ca^{2+} cations have a high affinity for alginate, while Mn^{2+} and Mg^{2+} have the lowest affinity.

2. Theoretical calculations

2.1. Model

Our model consists of an alginate chain composed of two M−blocks linked to two G-blocks through a GM glycosidic bond (Fig. 1). The torsion angle of each glycosidic bond present in the molecule was modified to obtain the lowest energy structure. Each structure was optimized by density functional theory (DFT) in the gas phase, with the B3LYP hybrid at the 6-31G (d, p) level of theory. Then, this structure was re-optimized in each metal understudy, modifying the distances and orientations towards the oxygens of the carboxylic group and the hydroxyl group present in the GG block until the

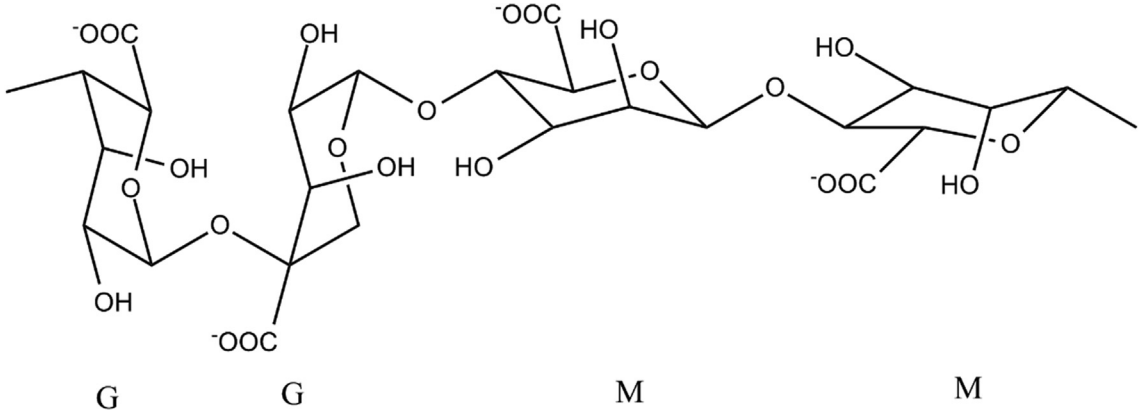

Fig. 1 Structure of blocks G and M of alginate.

lowest energy structure was obtained. The ALG-Cu (ALG-M: *ALG: alginate; M:* Cu^{2+}, Mn^{2+}, Ca^{2+}, Mg^{2+}) and ALG-Mn systems were optimized by effective central potential (ECP) with the LanL2DZ bases (Yang, 2009), while ALG-Mg and ALG-Ca with the Gaussian 6-31G (d, P) bases (Bekri, 2018).

3. Computational method

The optimization of the systems' geometry understudy, molecular orbital energy calculation, and global reactivity indexes were performed using G09 software. The calculations of the NCI index, ELF, populations, variance, relative flux, bond polarization, and visualization of the ELF diagrams and NBO orbitals were performed using Multiwfn 3.7 software. The VMD package was used to visualize the NCI isosurfaces, while the Chimera X 1.0 software was used to visualize the attractors' location. The NBO calculations were obtained using an internal module of G09.

The DFT is a mechano-quantum model in which the main factor is the electronic probability density, from which it is possible to determine the properties of systems composed of atoms and molecules. Within this model, it is possible to represent energy and any other property of the system by the number of electrons and the external potential. From this have emerged various indices of global and local reactivity. These indices arise from information obtained from orbital borders such as HOMO and LUMO (Obot et al., 2015). The global reactivity indexes used in this work are the following:

Electrophilicity ω: This index is a measure of the energy stabilization of the system when saturated with electrons that come from the environment.

$$\omega = \mu^2/2\eta \tag{1}$$

where μ is the chemical potential: This is a global property of the system in equilibrium so that electrons flow from regions of high chemical potential to regions of low chemical potential. This flow does not stop until the chemical potential is constant throughout the system. It is defined as:

$$\mu = (E_H + E_L)/2 \tag{2}$$

where E_H is the energy of the molecular orbital HOMO and E_L is the energy of the molecular orbital LUMO.

Hardnessη: This is a global property of the system and measures its resistance to the change in its electronic distribution. It is defined as:

$$\eta = (E_L - E_H)/2 \tag{3}$$

where $E_H$is the energy of the molecular orbital HOMO and $E_L$is the energy of the molecular orbital LUMO.

3.1. Reduced density gradient (RDG) and NCI index

To understand non-covalent interactions (NCI), of great interest in the chemical and physical properties of molecules, the reduced density gradient (RDG) is used (Boto et al., 2020). In this theory, the density Laplacian $\nabla^2 = \rho(r)$ decomposes into the sum of its contributions from the three eigenvalues λ_i of the Hessian matrix of the electron density at a given point, such that $\nabla^2\rho = \lambda_1 + \lambda_2 + \lambda_3$ being$\lambda_1 \leqslant \lambda_2 \leqslant \lambda_3$. The local virial theorem indicates that the main contributions to the potential energy V(r) (attractive) and the kinetic energy G(r) (repulsive) of the system are related to the eigenvalues of the Hessian at each point in space. The NCI index is based on the reduced density gradient (RDG) given by Eq. (4). This index is a dimensionless quantity used to describe the deviations from a homogeneous electronic distribution.

The RDG is determined as follows:

$$s = \frac{1}{2(3\pi^2)^{1/3}} \frac{|\nabla\rho(r)|}{\rho(r)^{4/3}} \tag{4}$$

The regions where the electron density λ_i and s have low values correspond to regions where non-covalent interactions occur.

Non-covalent interactions can be classified into different categories: electrostatics, π effects, van der Waals forces, and hydrophobic effects (Boto et al., 2020).

3.2. Natural bond orbital (NBO)

NBO analysis is a helpful method, widely described (Weinhold et al., 2016) and used to describe the nature of interactions between organic molecules with different metals (Lin et al., 2020) in terms of charge transfer from a filled orbital σ_i (electron donor) to the valence of an anti-bonding orbital σ_j^* (electron acceptor), resulting in so-called charge transfer or donor–acceptor interactions. This analysis method reveals important chemical information from the results obtained by transforming a wave function in the fundamental state, from which localized orbitals corresponding to the chemical notion of Lewis-type bonding are obtained. The interaction energy by charge transfer is called the second-order stabilization energy ($E^{(2)}$), which is estimated by the secondary perturbation theory, according to the following equation (Lu et al., 2019):

$$E_{i\to j}^{(2)} = -2\frac{\left\langle \sigma_i \middle| \widehat{F} \middle| \sigma_j^* \right\rangle}{\varepsilon_{j^*} - \varepsilon_i} \tag{5}$$

where $\widehat{F}$is the Fock operator of $\varepsilon_i = \left\langle \sigma_i \middle| \widehat{F} \middle| \sigma_i \right\rangle$, and $\varepsilon_{j^*} = \left\langle \sigma_j^* \middle| \widehat{F} \middle| \sigma_j^* \right\rangle$are the energies of the bonding naturals orbitals.

Additionally, it is possible to relate the magnitude of the Fock matrix elements to the bonding and anti-bonding orbitals' symmetry, which allows interpreting the energetic stabilization in terms of the generalized principle of maximum overlap between bonds and anti-bonds (Platts and Baker, 2020).

In this work, the concept of second-order stabilization energy ($E^{(2)}$) and natural bond orbital overlap will be used to try to describe the effect of the oxygen-metal interaction in the systems under study.

3.3. Electron localization function (ELF)

In quantum chemistry, the electron localization function (ELF) estimates the probability of finding an electron in the neighboring space of a reference electron located at a certain point and with the same rotation. The electron pair density provides the probability of finding an electron of a particular spin at a point in space when the second electron of the opposite spin is at a certain distance (Liu et al., 2018). Within this

context, the interpretation proposed by Savin et al. given by Eq. (6) indicates that the electron pair density can be generalized to any density-independent of spin (Fuentealba et al., 2007).

$$D = \frac{1}{2}\sum_{i}(\nabla\phi_i)^2 - \frac{1}{8}\frac{(\nabla\rho)^2}{\rho} \tag{6}$$

The first term on the right-hand side of Eq. (6) represents the kinetic energy density of the molecule under study, and the second term on the right-hand side is the von Weizsacker kinetic energy density which is exact for the hydrogen atom, exact for the helium atom in the HF approximation and exact for a boson system (Pilmé, 2017). Physically, this measures the extent of the spatial location of the reference electron and provides a method for mapping the probability of electron pairs in multielectronic systems. When applied to molecules, an ELF analysis shows a clear separation between the nucleus and the valence electron and shows covalent bonds and solitary pairs. As ELF is a scalar function, its gradient field's topological analysis determines local maxima (attractors) and the corresponding basins. The gradient vector field of ELF$\nabla\eta(\vec{r})$ allows dividing the Euclidean space into basins of attractors where electron pairs are located (Zhao et al., 2020). If the basin contains a nucleus (except a proton), it is a central basin (C). Otherwise, it is a valence basin (V). Invariably, a valence basin will be connected with at least one central basin. A vacancy representing a lone pair of electrons will be connected to a single central vacancy, and its attractor will be called monosynaptic. A basin representing a covalent bond will be connected with two central basins, and its attractor will be called disynaptic. Important properties of a chemical system can be examined by specific properties that basins exhibit, among those considered in this study are; the average population, the variance (σ^2), and the relative flux $\lambda\left(\bar{N};\Omega_i\right)$. The basin's population is obtained by integrating the electron density over the volume of the basin, according to Eq. (7). At the same time, σ2 represents the fluctuation of the electron pair, it is given by Eq. (8), and finally, the relative flux indicates the electron charge fluctuations for a given basin is described by Eq. (9) (Chauvin et al., 2016). Within this same context, the polarity of a bond can be determined by the model proposed by Raud and Jansen, based on the combination of the complementary topological partitions of the electron density, obtained from the theory of atoms in molecules (AIM) and the electronic localization function (ELF) (Raub and Jansen, 2001).

$$\bar{N}(\Omega_i) = \int_{\Omega_i}\sigma(r)dr = \bar{N}^{\alpha}(\Omega_i) + \bar{N}^{\beta}(\Omega_i) \tag{7}$$

$$\sigma^2(\Omega_A) = \int_{\Omega_A}\int_{\Omega_A}\Gamma_{XC}(\vec{r}_1,\vec{r}_2)d\vec{r}_1 d\vec{r}_2 + \bar{N}(\Omega_A) = \bar{N}(\Omega_A) - \lambda(\Omega_A) \tag{8}$$

$$\lambda_F(\Omega_A) = \frac{\sigma^2(\Omega_A)}{\bar{N}(\Omega_A)} \tag{9}$$

4. Results and discussion

4.1. Reactivity descriptors

As mentioned above, the electronic chemical potential characterizes the ability of a system to exchange electrons with the medium, where the electronic transfer occurs from the highest to the lowest potential. Table 1 shows that ALG-Cu and ALG-Mn have the highest electronic chemical potential. These results show that the interaction of Cu^{+2} and Mn^{+2} ions with the polymer makes the formed systems less susceptible to electron exchange with the medium, while the higher values shown by ALG-Ca and ALG-Mg indicate that the electron density of these systems can vary spontaneously (Fekri et al., 2020), which makes them more reactive. The principle of maximum hardness (PMH) states that molecular systems in equilibrium tend to high hardness states. This principle is defined as a measure of resistance to change in electron density. Therefore, the molecule's stability and reactivity are related to the chemical hardness (η) (Pearson, 1993). The hardness values (Table 1) show that ALG-Cu is the system with the highest value for this reactivity index, followed by ALG-Mn.

Furthermore, the systems formed with the metals Ca^{+2} and Mg^{+2} presented lower values. In this sense, the Ca^{+2} and Mg^{+2} ions form the least stable systems, where ALG-Ca would be the most reactive (Chandrasekaran and Kumar, 2015). Finally, the electrophilicity values indicate that the ALG-Ca and ALG-Mg systems are the ones that would tend to stabilize to a larger extent when accepting electron density from their environment, according to the definition of this reactivity index (Chattaraj and Giri, 2009). These values confirm the higher reactivity of these systems.

4.2. NCI

For the characterization of the bonds in the ALG-M systems, the theory of non-covalent interactions (NCI) was used. Binding and nonbinding interactions can be identified by the sign of the second Hessian eigenvalue (λ_2). The analysis results are shown in a graph of the reduced gradient of the density v/s the electronic density (ρ) multiplied by the signλ_2. The noncovalent/weak interactions are given by a low density; for example, Van der Walls interactions. The low density and low-density gradient that is$\lambda_2 < 0$, indicates strong attractive interactions (blue surface isosurface), attractive weak interactions (green surface isosurface), and $\lambda_2 < 0$ indicates steric repulsion (red isosurface) (Contreras-García et al., 2016). The NCI isosurfaces for the ALG-Cu and ALG-Mn systems are shown in Figs. 2a and 2b. These results indicate that the strongest metal-alginate interactions occur with atoms of the chain's outermost oxygens, corresponding to carboxylic acid functional groups (–COO^-) and hydroxyl groups (–OH). These oxygens are the closest and least sterically hindered; red and blue isosurfaces represent this in the form of rings on the metal–oxygen bond line.

Table 1 Global reactivity indices for ALG-Cu, ALG-Mn, ALG-Ca and ALG-Mg.

	ALG-Cu (eV)	ALG-Mn (eV)	ALG-Ca(eV)	ALG-Mg (eV)
μ	−0.75	−0.77	−4.31	−4.25
η	1.53	1.42	0.59	0.92
ω	0.18	0.21	52.49	9.77

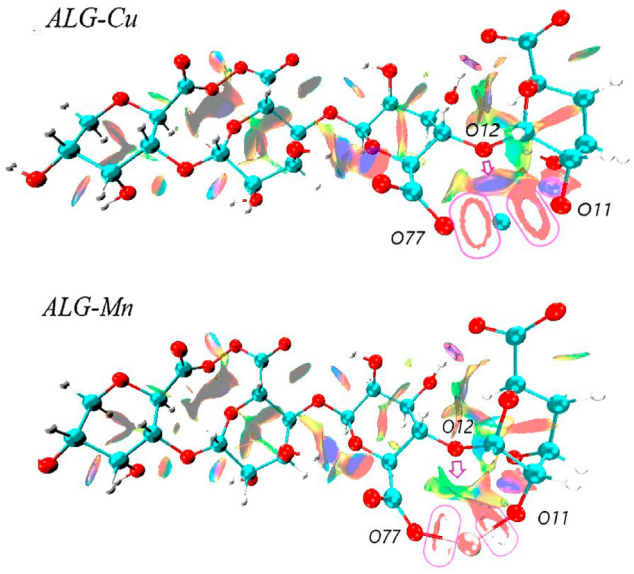

Fig. 2a Isosurfaces of the reduced density gradient with s = 0.6 a.u. for ALG-Cu and ALG-Mn.

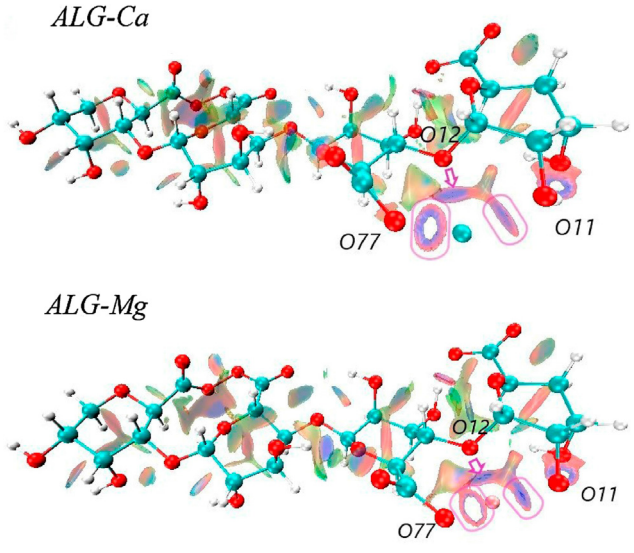

Fig. 2b Isosurfaces of the reduced density gradient with s = 0.6 a.u. for ALG-Ca and ALG-Mg.

The formation of such rings indicates that the electron density higher than 0.05 could not be appreciated, and only the weak interaction area is observed, i.e., the central (empty) area of the ring represents a strong bond (Lefebvre et al., 2017). The isosurfaces were obtained for an index $s = 0.6$, which accounts for an interesting difference. In the case of the ALG-Cu and ALG-Mn systems, these ring-shaped surfaces are fainter, concerning the systems with Ca and Mg. Moreover, the O_{77}-Mn and O_{11}-Mn interactions appear to be slightly stronger due to a lower electron density presence associated with weak bonds. Meanwhile, for the O_{77}-Ca bond, the ring-shaped isosurface is more closed, suggesting that the weakest O_{77}-M interaction occurs in the ALG-Ca system. It can also be seen that the O_{11}-Metal interaction is only strong in the presence of transition metals. As for the interaction of ether oxygen (-O-), which is the most sterically hindered, the isosurface show slight differences between systems. For example, in ALG-Mn, it is broad and shows a faint blue color, which accounts for the weakest O_{12}-M bonding of the systems under study.

Meanwhile, in ALG-Cu, the isosurface is of a more intense blue color and comprises a large area of the metal-binding region, which accounts for a stronger interaction. This description is very similar to that observed for the O_{12}-Mg and O_{12}-Ca bonds. Finally, intermolecular interactions are also observed, mainly by hydrogen bridges between the hydroxyl groups' hydrogens with neighboring oxygen atoms. According to the structural modifications that the polymer may undergo, these interactions vary in intensity due to their interaction with different metals. On the other hand, these results agree with those reported in previous experimental studies, where the strongest interaction between alginate and divalent metals occurs with the oxygen of the carboxyl group of the G-blocks (Lu et al., 2005). Also, our results show a strong interaction between the –OH groups with Cu^{2+} and Mn^{2+} ions.

4.3. NBO

4.3.1. NBO ALG-Cu

In Table 2, the NBO results for the ALG-Cu system are shown. This analysis predicts a σ (O_{77}-Cu) bond. The anti-bonding orbital σ*(O_{77} -Cu), formed by the p_y orbital of oxygen with the d_z^2orbital of copper, participates in different interactions that bring high stability to the structure (Zülfikaroğlu et al., 2018). The highest value of $E^{(2)}$ was for the interaction of LP 2 (O_{77}) (donor) with the anti-bonding orbital σ*(O_{77} -Cu) (acceptor), where the latter presents a high occupancy, which would give instability to the O_{77}-Cu bond (Lu et al., 2019). In Fig. 3A, the NBO orbitals for the anti-bonding orbital σ*(O_{77} -Cu) interactions with O_{11}, O_{12}, and O_{77} are shown. For the interaction between LP 2 (O_{77}) and σ*(O_{77} -Cu), the decrease of the donor density (green-yellow (positive) and violet (negative) region) and an increase of this in the anti-bonding orbital (green (positive) and blue (negative) region) are appreciated, generating a broad interaction region located around O_{77}, indicating a strong polarization of the bond (Lee et al., 2013). This interaction allowed reducing the energy of the system by 35.24 Kcal mol^{-1}. Another important

Table 2 Significant interactions (higher than 2.00 Kcal mol^{-1}) and their second-order perturbation energies $E^{(2)}$in the ALG-Cu system.

Donor (i)	Occupancy	Acceptor (j)	Occupancy	$E^{(2)}$ Kcal mol^{-1}
σ (C_6-O_{11})	1.99219	LP* *7* (Cu)	0.05719	2.91
σ (O_{11}-H_{42})	1.98884	LP* ***6*** (Cu)	0.09353	3.16
σ (O_{11}-H_{42})		LP* *7* (Cu)	0.05719	2.89
σ (C_{21}-O_{77})	1.99510	LP* *7* (Cu)		2.86
σ (C_{21}-O_{77})		σ*(O_{77} –Cu)	0.16663	3.26
σ* (C_{21}-O_{76})	0.29437	σ*(O_{77} –Cu)		3.45
LP ***1*** (O_{11})	1.96733	LP* *7* (Cu)	0.05719	4.39
LP ***1*** (O_{11})		LP* ***8*** (Cu)	0.03830	2.13
LP ***2*** (O_{11})	1.86336	LP* ***6*** (Cu)	0.09353	18.25
LP ***2*** (O_{11})		LP* *7* (Cu)	0.05719	10.31
LP ***2*** (O_{11})		σ*(O_{77}-Cu)	0.16663	24.36
LP ***1*** (O_{12})	1.95326	LP* ***6*** (Cu)	0.09353	2.14
LP ***1*** (O_{12})		LP* ***8*** (Cu)	0.03830	3.10
LP ***2*** (O_{12})	1.89306	LP* ***6*** (Cu)	0.09353	2.34
LP ***2*** (O_{12})		LP* ***8*** (Cu)	0.03830	4.79
LP ***2*** (O_{12})		σ*(O_{77} –Cu)	0.16663	3.20
LP ***1*** (O_{77})	1.93078	LP* *7* (Cu)	0.05719	9.19
LP ***2*** (O_{77})	1.80574	LP* ***6*** (Cu)	0.09353	2.74
LP ***2*** (O_{77})		LP* *7* (Cu)	0.05719	16.78
LP ***2*** (O_{77})		σ*(O_{77} –Cu)	0.16663	35.24
LP ***5*** (Cu)	1.98263	σ*(O_{77} –Cu)		3.12

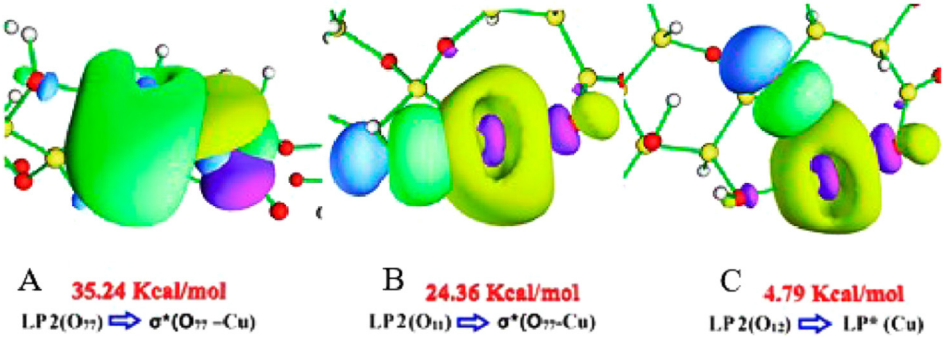

Fig. 3 ABC NBO orbitals for the most important interactions, in terms of $E^{(2)}$, in ALG-Cu.

interaction was LP 2 (O_{77}), with the anti-bonding orbital σ* (O_{77} -Cu). This interaction presented the second-highest value of $E^{(2)}$. The σ*(O_{77} -Cu) acts as an acceptor of LP 2 (O_{11}) (donor), of low occupancy, a product of electronic donation to the anti-bonding orbital, thus decreasing its instability due to its high occupancy. NBO orbitals represent this interaction in Fig. 3B. Here, it is observed how the donor's positive density regions (LP 2 (O_{11})) and the acceptor generate a region of interaction smaller than that visualized with O77, which is expressed in a lower value of $E^{(2)}$. For O_{12}, the perturbation energy values were lower. In Fig. 3C, the NBO orbitals of the interaction between LP 2 (O_{12}) and σ*(O_{77} -Cu) can be observed. The overlap of the orbital of the lone pair of O_{12} with the σ* of the O_{77}-Cu bond is low. The sum of the perturbation energies was 63.95 Kcal mol^{-1} for O_{77}-Cu, for O_{11}-Cu 59.44 Kcal mol^{-1} and for O_{12}-Cu 15.57 Kcal mol^{-1}. The above is related to that indicated by the NCI isosurfaces, which show a slightly stronger interaction with O_{77}.

4.3.2. NBO ALG-Mn

Table 3. Presents the NBO results for the ALG-Mn system. The NBO analysis predicts the O_{77}-Mn bond formed by an $d(x^2 - y^2)$orbital of manganese to the *px* orbital of oxygen. The σ-bonding orbital (O_{77}-Mn) acts as a donor, and the anti-bonding π* (C_{21}-O_{76}) as an acceptor, which generated a high structural stabilization, with one of the highest values $E^{(2)}$ (38.22 Kcal mol^{-1}). The donor orbital occupancy is low, while that of the acceptor is high, revealing a strong charge transfer. The fact that the occupancy in the anti-bonding orbital is high decreases the stability of the C_{21}-O_{76} bond (Raju et al., 2020), of which O_{77} is a part. Furthermore, the anti-bonding orbital σ* (O_{77}-Mn) acts as an acceptor in several

Table 3 Significant interactions (higher than 2.00 Kcal mol^{-1}) and their second-order perturbation energies $E^{(2)}$ in the ALG-Mn system.

Donor (i)	Occupancy	Acceptor (j)	Occupancy	$E^{(2)}$ Kcal mol^{-1}
σ (C_6-O_{11})	1.99154	LP* ***4*** (Mn)	0.16684	3.18
σ (O_{11}-H_{42})	1.98906	LP* ***4*** (Mn)		3.99
σ (O_{11}-H_{42})		LP* ***6*** (Mn)	0.04227	2.55
σ (C_{21}-O_{77})	1.99362	σ* (O_{77}-Mn)	0.07984	2.77
σ (O_{77}-Mn)	1.80640	π* (C_{21}-O_{76})	0.25870	38.22
π* (C_{21}-O_{76})	0.25870	σ* (O_{77}-Mn)	0.07984	8.44
LP ***1*** (O_{11})	1.94344	LP* ***6*** (Mn)	0.04227	3.34
LP ***1*** (O_{11})		σ* (O_{77}-Mn)	0.07984	4.62
LP ***2*** (O_{11})	1.84993	LP* ***4*** (Mn)	0.16684	50.57
LP ***2*** (O_{11})		LP* ***5*** (Mn)	0.13032	4.00
LP ***2*** (O_{11})		LP* 6 (Mn)	0.04227	7.69
LP ***2*** (O_{11})		σ* (O_{77}-Mn)	0.07984	10.00
LP ***1*** (O_{12})	1.95808	LP* 7 (Mn)	0.02868	1.37
LP ***2*** (O_{12})	1.89984	LP* 7 (Mn)		1.35
CR ***1*** (O_{77})	1.99970	RY* ***2*** (Mn)	0.01064	2.73
LP ***1*** (O_{77})	1.88007	LP* ***4*** (Mn)	0.16684	10.51
LP ***1*** (O_{77})		LP* ***5*** (Mn)	0.13032	2.57
LP ***1*** (O_{77})		LP* ***6*** (Mn)	0.04227	10.73
LP ***2*** (O_{77})	1.80832	LP* ***5*** (Mn)	0.13032	30.68
LP ***2*** (O_{77})		LP* ***6*** (Mn)	0.04227	3.55
LP ***2*** (O_{77})		σ* (O_{77}-Mn)	0.07984	14.22

stabilizing system interactions. Among these were those of LP 2 (O_{77}) and LP 2 (O_{11}), which transfer charge to the anti-bonding orbital, generating moderate values of $E^{(2)}$. Another interaction to consider was the anti-bonding orbital π* (C_{21}-O_{76}) with σ* (O_{77}-Mn). The former presented a high occupancy, as already mentioned. The charge transfer performed by π* (C_{21}-O_{76}) would allow it to decrease the bond instability of the carboxylic group of O_{77}. In Fig. 4, the NBO orbitals are shown for the interactions that presented high values of$E^{(2)}$. Among these are those involving σ (O_{77}-Mn) and π* (C_{21}-O_{76}). In the σ → π* donation, a broad region of interaction is observed, where there is a decrease in density in the donor (green and blue colored surfaces) and an increase in density in the acceptor, indicating charge transfer (Fig. 4A). In the interactions in which σ* acts as an acceptor for LP 2 (O_{11}) and LP 2 (O_{77}) (Fig. 4B and 4C), the overlap decreases, leading to a drop in the perturbation energy values. Meanwhile, the interaction LP 2 (O_{11}) (donor) and $sp^3(75\% caracter - p)$ LP* 4 (Mn) (acceptor), where the d_z^2orbital of Mn and the hybrid $p_y$orbital of the sp^3 hybridization

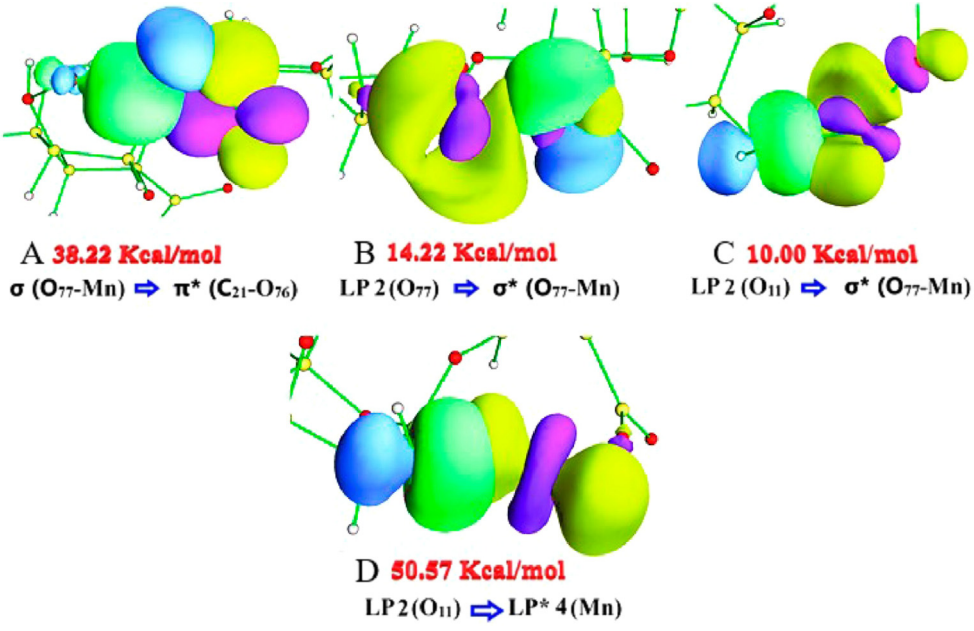

Fig. 4 ABC NBO orbitals for the most important interactions, in terms of $E^{(2)}$, in ALG-Mn.

oxygen (75% character-p), present a high overlap, generating the highest value of $E^{(2)}$ (50.57 Kcal mol^{-1}) (Fig. 4D). Meanwhile, the interaction between LP 2 (O_{77}) (donor) and LP* 5 (Mn) (acceptor) presented the third highest value of $E^{(2)}$ due to a strong charge transfer from donor to acceptor. For O_{12}-Mn, lower values of , were obtained where LP 1 (O_{12}) and LP 1 (O_{12}) transfer charge to LP* (Mn). The latter presented the lowest occupancy value concerning the other anti-bonding orbitals presented in Table 3. The latter suggests little charge transfer resulting in a very weak interaction between O_{12} and the metal. The sum of $E^{(2)}$ for O_{77}-Mn was 74.99 Kcal mol^{-1}, for O_{11}-Mn 80.22 Kcal mol^{-1}, and for O_{12}-Mn was 2.72 Kcal mol^{-1}. Finally, the perturbation energy values for the O_{77}-Mn and O_{11}-Mn bond presented higher values than in ALG-Cu, which agrees with the NCI isosurfaces, suggesting that the O_{77}-Mn and O_{11}-Mn interaction would be slightly stronger than O_{11}-Cu and O_{77}-Cu, while with O_{12}, copper presents a stronger interaction.

4.3.3. NBO ALG-Mg

Table 4 shows the NBO results for the ALG-Mg system. This analysis predicted an O_{77}-Mg bond. The highest value of $E^{(2)}$ was for the interaction between σ (O_{77}-Mg) and π* (C_{21}-O_{76}) (47.81 Kcal mol-1), where, according to the occupancy values of the donor and acceptor, there is a strong charge transfer, which would weaken the C_{21}-O_{76} bond, due to the high occupancy of the π* orbital. This bond would decrease its instability by charge transfer to LP* 2 (Mg). This interaction's high stability is due to the delocalization of the electronic density in the carboxylic group. In Fig. 5A, the NBO orbitals for the σ → π* interaction are shown. A high overlap is observed, giving rise to a π interaction, where there is a decrease in the donor density (green–blue surfaces) and even an increase in that of the acceptor (green-yellow-violet surfaces), indicating the strong charge transfer already mentioned. The interaction of LP 2 (O_{11}) with LP* 2 (Mg) generates the highest value $E^{(2)}$for the interaction between O_{11} and Mg (17.03 Kcal mol-1), but lower than those obtained in the ALG-Cu and ALG-Mn systems, where there is charge transfer from an n to an n* orbital. The latter showed a moderate occupancy value. This interaction is visualized through NBO orbitals in Fig. 5B. In this, an overlap σ, between the hybrid orbital *pz* of LP 2 (O_{11}), of hybridization $sp^{2.76}$ with 73% -*p* character, with the pz orbital of LP* 2 (Mg) of hybridization $sp^{99.99}$and 99.35% p-character, is seen. The predicted interactions for O_{12} differ from the previous systems analyzed in that these generate higher stability with the metal. The highest value of $E^{(2)}$, obtained for this interaction, was 14.78 Kcal mol-1, where the donor occupancy is low (LP 2 (O_{12})), and the acceptor occupancy is high (LP* 1 (Mg)), accounting for the strong charge transfer. Fig. 5C shows the NBO orbitals for LP 2 (O_{12}) interaction with LP* 1 (Mg). The *py* hybrid orbital of the oxygen lone pair, of hybridization $sp^{3.75}$ with 79% -*p* character overlaps with the *px* orbital of the n*, which presents an increase in the density region, the product of the charge transfer. Then, O_{77} presents the highest value of $E^{(2)}$ for the interaction between LP 2 (O_{77}) and LP* 2 (Mg) (18.57 Kcal mol^{-1}), where the donor and acceptor occupancy values suggest a low charge transfer. It is highlighted that O_{77} generates a higher amount of stabilizing interactions, as shown in Table 4. Nevertheless, given the perturbation energy values, the O_{77}-Mg interactions are smaller than those observed with Cu^{2+} and Mn^{2+}. NBO orbitals represent this interaction in Fig. 5D. An overlapping σ is appreciated between the hybrid py orbital of LP 2 (O_{77}) of hybridization $sp^{3.19}$with 78% -*p*character and the *pz* orbital of LP* (Mg), with 99.35% p-character. Finally, an LP* 1 (Mg) interaction with σ* (O_{77}-Mg) generates a low charge transfer to the anti-bonding sigma orbital. Therefore,

Table 4 Significant interactions (higher than 2.00 Kcal mol^{-1}) and their second-order perturbation energies $E^{(2)}$in the ALG-Mg system.

Donor (i)	Occupancy	Acceptor (j)	Occupancy	E(2) Kcal mol^{-1}
σ (C_6-O_{11})	1.99123	LP* ***2*** (Mg)	0.08039	2.43
σ (O_{11}-H_{42})	1.98855	LP* ***2*** (Mg)		3.56
σ (O_{12}-H_{13})	1.98812	LP* ***1*** (Mg)	0.05227	2.07
σ (C_{21}-O_{77})	1.99316	LP* ***2*** (Mg)	0.08039	2.96
σ (O_{77}-Mg)	1.80464	π* (C_{21}-O_{76})	0.22042	47.81
CR ***1*** (O_{11})	1.99984	LP* ***2*** (Mg)	0.08039	2.26
LP ***1*** (O_{11})	1.96682	LP* ***3*** (Mg)	0.05227	2.69
LP ***2*** (O_{11})	1.90001	LP* ***1*** (Mg)	0.13797	6.80
LP ***2*** (O_{11})		LP* ***2*** (Mg)	0.08039	17.03
LP ***2*** (O_{11})		LP* ***3*** (Mg)	0.05227	6.85
LP ***1*** (O_{12})	1.94652	LP* ***1*** (Mg)	0.13797	5.59
LP ***1*** (O_{12})		LP* ***2*** (Mg)	0.08039	2.66
LP ***2*** (O_{12})	1.89639	LP* ***1*** (Mg)	0.13797	14.78
LP ***2*** (O_{12})		LP* ***2*** (Mg)	0.08039	3.01
LP ***2*** (O_{12})		LP* ***3*** (Mg)	0.05227	8.03
LP ***2*** (O_{12})		σ* (O_{77}-Mg)	0.08384	9.91
CR ***1*** (O_{77})	1.99979	LP* ***2*** (Mg)	0.08039	2.81
LP ***1*** (O_{77})	1.93189	LP* ***2*** (Mg)	0.08039	10.47
LP ***2*** (O_{77})	1.85541	LP* ***1*** (Mg)	0.13797	15.89
LP ***2*** (O_{77})		LP* ***2*** (Mg)	0.08039	18.57
LP ***2*** (O_{77})		σ* (O_{77}-Mg)	0.08384	10.14
LP* ***1*** (Mg)	0.13797	σ* (O_{77}-Mg)		2.73

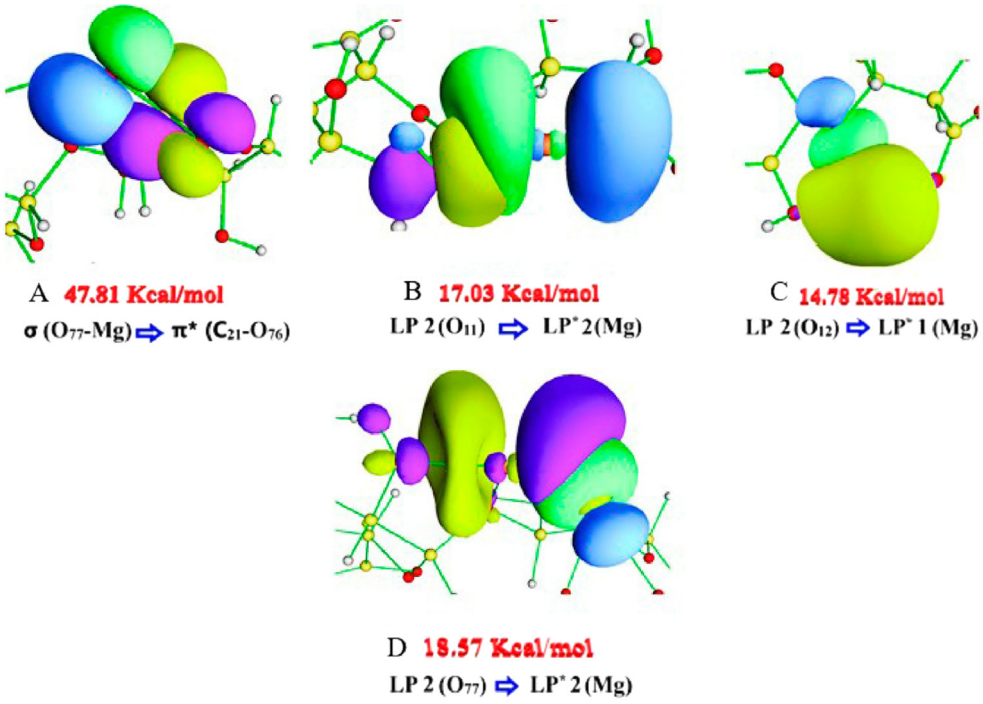

Fig. 5 ABC NBO orbitals for the most important interactions, in terms of $E^{(2)}$, in ALG-Mg.

the O_{77}-Mg bond stability is less affected; the O_{12}-Mg interaction results in higher stability than that generated with Cu^{2+} and Mn^{2+}, due to the ionic radius of Mg^{2+} (the smallest of the metals under study) and its low electron density. The sum of $E^{(2)}$for the O_{77}-Mg interaction was 57.88 Kcal mol^{-1}, for O_{11}-Mg 33.37 Kcal mol^{-1}, and for O_{12}-Mg 43.98 Kcal mol^{-1}. These results agree with those given by the NCI index, which indicates that Mg interacts more weakly with O_{77} and O_{11}, concerning Cu^{2+} and Mn^{2+}, while the binding with O_{12} is stronger for Mg^{2+}. On the other hand, the most stabilizing interaction, which corresponds to the charge transfer from the σ bond (O_{77}-Mg) to π* (C_{21}-O_{76}), suggests that the electronic delocalization produced in the carboxylic group would be the one that most stabilizes the O_{77}-Mg interaction.

4.3.4. NBO ALG-Ca

Table 5 presents the NBO results for ALG-Ca. The NBO analysis did not predict any O-Ca bonds. Calcium interactions with oxygens occur through charge transfer from LP 2 (O_{11}), LP 2 (O_{12}), and LP 2 (O_{77}) lone pairs to LP* 1 (Ca). The values $E^{(2)}$ for the O_{11} interaction with Ca are low and lower than the systems already analyzed. The highest value obtained was for LP 2 (O_{11}) and LP* 1 (Ca) (7.41 Kcal mol^{-1}), where the occupancy of this LP* 1 (Ca) is the highest and it is the one that participates as an acceptor in the most stabilizing interactions with the three oxygens under study. Fig. 6A shows the NBO orbitals for the interactions, as mentioned earlier. In these, it can be observed how the localized orbitals of LP 2 (O_{11}), LP 2 (O_{12}), and LP 2 (O_{77}) interact with LP* 1 (Ca), which presents an increase in its density region as a result of the charge transfer of the mentioned oxygens (Fig. 6A). The interaction LP 2 (O_{77}) and LP* 1 (Ca) produced the highest value of hyperconjugative interaction energy $E^{(2)}$ (11.28 Kcal mol^{-1}). In Fig. 6B, the frontal overlap between the NBO orbitals involved in this interaction is observed. In the same image, the NBO orbitals for the interaction that generated the highest value between O_{12} and the metal (5.01 Kcal mol^{-1}) can be noticed (Fig. 6C). In this case, there is a sigma overlap between the n orbital of LP 2 (O_{12}) and the aforementioned n* orbital of calcium. The interactions where calcium acts as a donor were not considered in the table because they have low $E^{(2)}$values. The sum of the values $E^{(2)}$ for O_{77}-Ca was 41.96 Kcal mol^{-1}, O_{11}-Ca 23.65 Kcal mol^{-1}, and O_{12}-Ca 16.85 Kcal mol^{-1}. This analysis reveals that the O-metal interactions for ALG-Ca, considered mainly as O → Mg charge transfer, generate little stability to the structure and lower electronic delocalization concerning ALG-Cu and ALG-Mn.

4.4. ELF topological analysis

4.4.1. ALG-Cu

We will try to deepen the nature of bonding by employing ELF topological analysis and attractor analysis. Fig. 7A shows the diagrams of the electronic localization function and the monosynaptic attractors, which correspond to the nonbonding electrons of the oxygen atoms interacting with the metal and their respective populations for the different systems under study. Table 6 shows these populations, variance, and relative flux, where, also, attractors of other oxygens present in the system are considered. High ELF values (approximately 0.8–1.0) are red; intermediate ELF values are represented by orange, green, and blue regions. The lower end of the scale is represented by white. The analysis of the attractors tells us that if the position of the attractor tends to be between the centers (bond line), the covalence increases until a completely symmetrical topology is achieved (pure covalent bond) (Savin et al.,

Table 5 Significant interactions (greater than 2.00 Kcal mol^{-1}) and their second-order perturbation energies $E^{(2)}$in the ALG-Ca system.

Donor (i)	Occupancy	Acceptor (j)	Occupancy	E(2) Kcal mol^{-1}
LP *2* (O_{11})	1.94508	LP* *3* (Ca)	0.04333	3.78
LP *2* (O_{11})		LP* *4* (Ca)	0.02629	4.34
LP *2* (O_{11})		LP* *1* (Ca)	0.10299	7.41
LP *2* (O_{11})		LP* *3* (Ca)	0.04333	3.78
LP *2* (O_{11})		LP* *4* (Ca)	0.02629	4.34
LP *1* (O_{12})	1.95197	LP* *1* (Ca)	0.10299	4.05
LP *1* (O_{12})		LP* *3* (Ca)	0.04333	2.68
LP *1* (O_{12})		LP* *4* (Ca)	0.02629	2.26
LP *2* (O_{12})	1.92360	LP* *1* (Ca)	0.10299	5.01
LP *2* (O_{12})		LP* *4* (Ca)	0.02629	2.85
LP *1* (O_{77})	1.94007	LP* *1* (Ca)	0.10299	9.41
LP *1* (O_{77})		LP* *2* (Ca)	0.04468	2.15
LP *1* (O_{77})		LP* *3* (Ca)		8.45
LP *2* (O_{77})	1.89529	LP* *1* (Ca)	0.10299	11.28
LP *2* (O_{77})		LP* *3* (Ca)	0.04333	4.60
LP *3* (O_{77})	1.73465	LP* *2* (Ca)	0.04468	2.92
LP *3* (O_{77})		LP* *5* (Ca)	0.02029	3.15

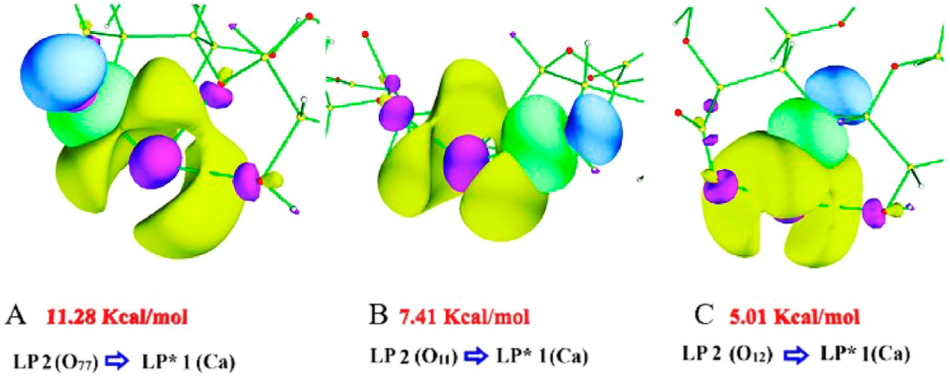

Fig. 6 ABC NBO orbitals for the most important interactions, in terms of$E^{(2)}$, in ALG-Ca.

1997). The copper atom presents the core's degenerate attractors with a total electronic population of 27.75e, lower than the expected value of 28e (isolated atom); this would result from the 3d contribution to the valence region (Fuster et al., 2004). There are also delocalized valence attractors in the outermost region of the copper atom (V (Cu), V' (Cu), and V'' (Cu)), with low electronic populations. This is related to the low delocalized electron density between O_{11}-Cu-O_{77}, represented in the ELF diagram (Fig. 7B), by the blue-colored region surrounding O_{77}, Cu, and O_{11}, to a lesser extent O_{12} (Fig. 7C). The ELF value is 0.40, lower than the homogeneous gas reference value, indicating high electronic delocalization in the mentioned region (Jerabek et al., 2018). It is observed as the attractors of the lone pairs V (O_{11}), V (O_{12}), and V (O_{77}) are oriented towards the metal, and their electronic populations are low if compared to the respective attractors present in this system Table 6. On the other hand, the attractors representing the other lone pair of these oxygens (V' (O_{11}), V' (O_{12}), and V' (O_{77})) have higher populations if the same comparison is made. The former indicates electronic donation from the oxygens to the metal, and the latter is explained by an asymmetric redistribution of the electron density generated by charge transfer from the metal (Durlak et al., 2009). The monosynaptic basin V (O_{11}) (highlighted in Fig. 7) is located at the junction line between O_{11} and Cu (binding distance of 1.95 A^0), with a low electron population of 2.06e (the average value was 2.32e) (Table 6). The total population for V (O_{11}) and V'(O_{11}) was 4.72e, which is below the average for other basins of lone pairs of oxygens of the same type in this system (4.75e), suggesting electron density donation $O_{11} \rightarrow$ Cu (Chaudret et al., 2011). According to Silvi & Savin, the position of V (O_{11}) can be interpreted, as a dative covalent bond type, where the pair of electrons forming this bond are contributed by oxygen; this is also supported by the high value of σ^2, which indicates a high electronic delocalization in the metal-binding region (Savin et al., 1996). On the other hand, the ELF diagram (Fig. 7B) shows us that the non-bonding pair of O_{77} and O_{11} interacting with copper are oriented towards the metal and present high delocalization (orange region), mainly O_{77}. The monosynaptic basin V (O_{12}) is oriented towards copper, close to the binding line, with a population of 2.33e (lower value than the average of 2.46e), indicating charge transfer $O_{12} \rightarrow$ Cu. The total population for V (O_{12}) and V' (O_{12}) was 5.00e (higher than average), suggesting

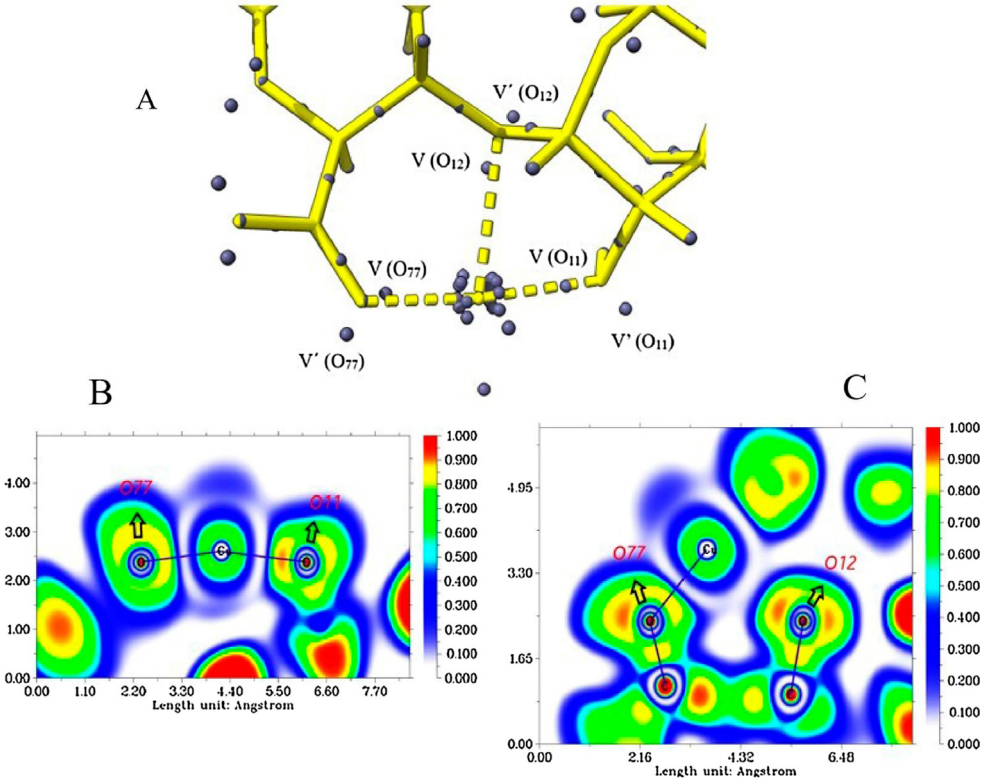

Fig. 7 Attractor populations of the lone pairs of O_{11}, O_{12}, O_{77} and valence attractors and the copper core (A). ELF diagrams for the Cu-(O_{77}, O_{11}) interaction (B), and for the Cu-(O_{12}, O_{77}) interaction (C).

Table 6 Populations (N), variance (σ^2), relative flux ($\lambda_{(\bar{N};\Omega_i)}$), for O_{11}, O_{12}, and O_{77} attractors and average populations ($\bar{N}$), variance ($\bar{\sigma}^2$), and relative flux ($\bar{\lambda}_{(\bar{N};\Omega_i)}$) of other oxygen attractors of Alcohol, carboxylic acid, and ether, present in ALG-Cu.

Attractor ALG-Cu	*Populations* $\frac{\bar{N}}{N}$*OH/, –CO/, -O-*			$\bar{\sigma}^2/\sigma^2$*–OH/, –CO/, -O-*			$\bar{\lambda}_{(\bar{N};\Omega_i)}/\lambda_{(\bar{N};\Omega_i)}$ *(–OH/, –CO/, -O-)*		
$\bar{V}$(O)	2.32e	2.65e	2.43e	0.28	0.66	0.86	0.22	0.43	0.36
$\bar{V}$(O)	2.43e	2.80e	2.49e	0.47	1.23	1.17	0.27	0.27	0.47
V (O)	**2.06e**	**2.46e**	**2.33e**	**1.13**	**1.27**	**1.18**	**0.55**	**0.52**	**0.50**
V(O)	**2.67e**	**3.47e**	**2.67e**	**1.19**	**1.42**	**1.23**	**0.45**	**0.41**	**0.46**

Cu → O_{12} charge transfer. The high electron flux, given by the value of σ^2, suggests that a high electron density (concerning the total population of this attractor) is delocalized, but not in the direction of binding to Cu, as suggested by its localization; this can be observed in the ELF diagrams, where the Cu-O_{12} interaction region presents an ELF value close to zero. Considering also that the binding distance was 2.48 A^0, it is suggested that the O_{12}-Cu interaction is mainly electrostatic. The position of the monosynaptic basin V (O_{77}) is similar to that of V (O_{11}), with a population of 2.46e (low value to the average of 2.73e), while V' (O_{77}) 3.47e (high value), and between them, they add up to the highest population (5.93e), concerning the average ($\bar{N}$ = 5.45e). The O_{77}-Cu bond distance was 1.84A^o. The attractor's location and populations and the short binding distance suggest that electron density donation and back-donation phenomena between O_{77} and copper give a covalent character; this is also reflected in the variance (σ^2)) value, indicating a considerable increase of electronic flux in the bonding region.

Meanwhile, the high electron population in V' (O_{77}) suggests that this lone pair contributes to the π C_{21} = O_{77} bond. Finally, the analysis of the relative basin fluctuation (Table 6) shows us a high electronic delocalization in O_{11}, O_{12}, O_{77}, and Cu. These high values suggest that this interaction could be represented by a system where the charge supported by each atom involved in the interaction varies continuously in time, in the manner of a resonant structure (Poater et al., 2005). This is in agreement with the hyperconjugative energy values $E^{(2)}$ of the NBO analysis. It is suggested that this system's chemical stability would be related to the electronic delocalization produced in the oxygen-metal interaction. Finally, the atomic contributions to the V (O) localization basins are analyzed below. The V (O_{11}) contribution is given by 95.60% contributed by the oxygen lone pair and 4.4% by Cu. That is, of the total

2.06e, 1.96e are contributed by oxygen and only 0.1e by copper. For V (O_{77}), the contributions are given by 94.51% of the lone pair of O_{77} and 5.50% of Cu; therefore, 2.32e are contributed by O_{77} and 0.14 by copper. According to several authors, the above agrees with the interpretation of an O → Cu dative bond (Mierzwa et al., 2020). These results indicate that these bonds are strongly polarized. The high populations of V (O_{77}) and V' (O_{77}) could be explained by the high electronic delocalization of the carboxylic group, as shown by NBO results and ELF attractor analysis. The V (O_{12}) contributions are given by 98.90% O_{12} and 1.1% Cu in terms of populations indicating that O_{12} and only 0.03e by Cu contribute 2.3e; this is related to the lower interaction between O_{12} and the metal, which corresponds with the idea of electrostatic interaction.

4.4.2. ALG-Mn

Fig. 8 shows the attractors and ELF diagrams for the interaction between O_{11}, O_{12}, and O77 with Mn. In the ELF diagrams (Fig. 8A and 8B), the nonbonding electron pairs of the oxygens, the core electrons, and the Mn atom's valence electrons can be observed. Also, a region with delocalized electron density can be observed with ELF values close to 0.4, distributed between Mn-O_{77} and to a lesser extent with O_{11}, similar to that described in the ALG-Cu system. On the other hand, Table 7 shows the average values of populations, variance (σ^2), and relative fluctuation $\lambda\left(\bar{N};\Omega_i\right)$ for the monosynaptic oxygen attractors (lone pairs); O_{11}, O_{12}, and O_{77}. The total population for the core attractors was 20.27e, well below the formal value of 23e; this would indicate the contribution of 3d electrons to the valence region (Mierzwa et al., 2018). For the lone pair attractors of O_{11} and O_{77}, the same trend seen in the ALG-Cu system is observed in terms of decreasing the metal-oriented lone pairs populations and the asymmetric electron density distribution. V (O_{11}) presents the lowest electron population (2.14e for an average of 2.32e). The total population for V (O_{11}) and V' (O_{11}) was 4.69e, a low value compared to the average (4.74e).

Additionally, the bond length was 1.97 A^0. The above and the localization of V (O_{11}) suggest that this interaction presents some covalent character, where the electron density donation from O_{11} to Mn would be the dominant process; this agrees with the interpretation of Silvi et al. regarding the nature of the dative bond concerning the attractor's position. The idea of the degree of covalence of this bond is also supported by the high electronic flux given by σ^2 (a higher value for this type of oxygens in the ALG-Mn system, considering its low population), which would be evidencing the high delocalization, product of the electronic exchange between these nuclei. The V attractor (O_{77}) is oriented towards the metal and located near the bond line. It presents a low population of 2.48e for an average of 2.69e, indicating a donation from O_{77} to the metal. The sum of the populations of V (O_{77}) and V' (O_{77}) was 5.88e, higher than the average (5.38e).

Meanwhile, the bond length was 1.81 A^0. The short binding distance, the orientation of V (O_{77}), and the population analysis suggest some covalent nature via both donating and back-donating processes. The ELF diagrams (Fig. 8A and 8B) show the lone pairs of O_{77} highly delocalized, and an

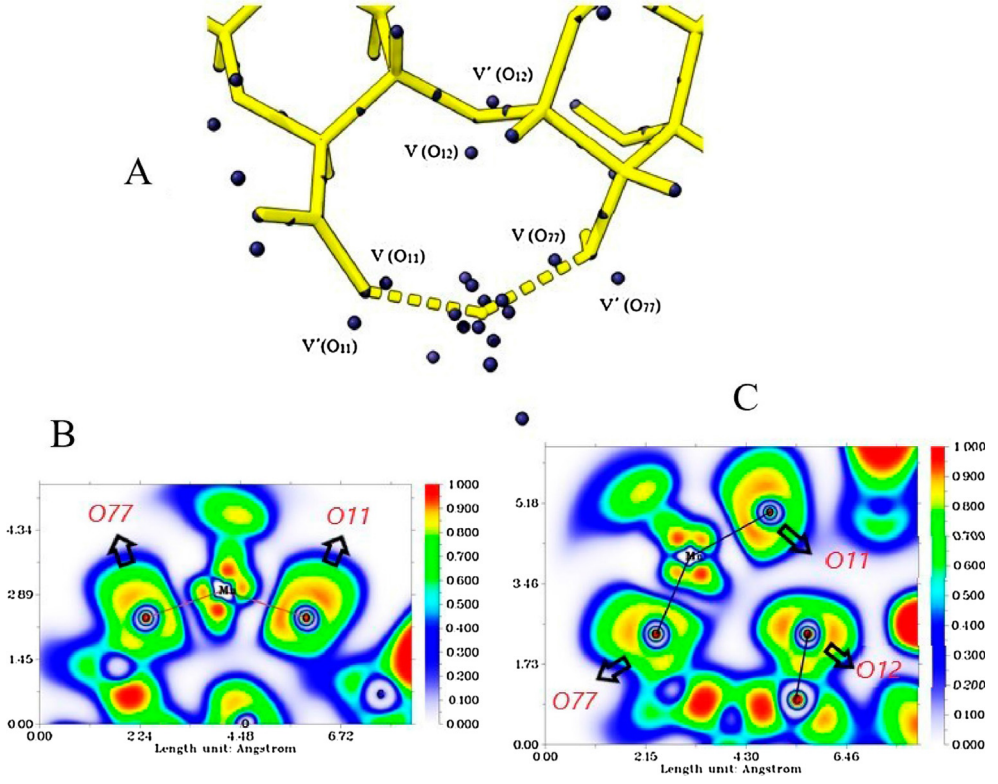

Fig. 8 Attractor populations of the lone pairs of O_{11}, O_{12}, O_{77} and valence, and core attractors of manganese (A). ELF diagrams for the Mn-(O_{77}, O_{11}) interaction (B) and for the Mn-(O_{11}, O_{12}, O_{77}) interaction (C).

Table 7 Populations (N), variance (σ^2), and relative flux ($\lambda_{(\bar{N};\Omega_i)}$), for O_{11}, O_{12}, and O_{77} attractors and average populations ($\bar{N}$), variance ($\bar{\sigma}^2$), and relative flux ($\bar{\lambda}_{(\bar{N};\Omega_i)}$) of other oxygen attractors of Alcohol, carboxylic acid, and ether, present in ALG-Mn.

Atractor ALG-Mn	*Poblaciones* $\bar{N}/N$–*OH*/, –*CO*/, -*O*-			$\bar{\sigma}^2/\sigma^2$–*OH*/, –*CO*/, -*O*-			$\bar{\lambda}_{(\bar{N};\Omega_i)}/\lambda_{(\bar{N};\Omega_i)}$ (–*OH*/, –*CO*/, -*O*-)		
$\bar{V}$(O)	2.32e	2.60e	2.43e	1.11	1.17	1.22	0.48	0.46	0.48
$\bar{V}$(O)	2.43e	2.78e	2.50e	1.12	1.21	1.18	0.46	0.43	0.39
V (O)	**2.14e**	**2.48e**	**2.41e**	**1.14**	**1.24**	**1.18**	**0.53**	**0.50**	**0.49**
V(O)	**2.55e**	**3.40e**	**2.56e**	**1.18**	**1.43**	**1.21**	**0.46**	**0.42**	**0.47**

interaction region encompassed by the aforementioned non-bonding electron density is appreciated. On the other hand, the high value of σ^2shows a high electronic flux due to the exchange of electrons between both elements. On the other hand, the high population of V' (O_{77}) (3.40e) suggests that it contributes to the π C_{21} = O_{77} bond, as described in ALG-Cu. V' (O_{12}) is oriented toward Mn but not in the bond line, which has a length of 3.03 A^0. The populations of V (O_{12}) and V' (O_{12}) are closer to the average values (Table 7), indicating a lower interaction between O_{12} and Mn.

On the other hand, the ELF diagram shows that the bonding region between O_{12} and Mn presents an ELF value close to zero, and no delocalized electron density shared with the other atoms understudy is observed. This value is also reflected in the variance, which presented a low value (Table 7), i.e., the pair of nonbonding electrons that interact with Mn are largely located in O_{12}; the values of the relative fluctuation confirmed this, showing a high electronic delocalization between O_{11}-Mn-O_{77}. Meanwhile, the value of $\lambda\left(\bar{N};\Omega_i\right)$ obtained for O_{12} is within the average, confirming that the charge would be more localized on the O_{12} atom, which reaffirms the description of weak electrostatic bonding. The analysis of contributions to the V (O) basin yielded the following results: V (O_{11}) = 98.08% (2.10e) O_{11}; Mn = 1.92% (0.04e), for V (O_{77}) = 97.78% (2.43e) and 2.22% (0.05e). These results have the same interpretation given for these attractors in the ALG-Cu system. That is, bonds of dative character, highly polarized between copper with O_{11} and O_{77}. For V (O_{12}), a contribution of 100% O_{12} was obtained, which confirms the scarce interaction between this oxygen and manganese.

4.4.3. ALG-Mg

In Fig. 9, the ELF diagrams, the attractors, and their electronic populations in the ALG-Mg system are presented. In Fig. 9B and 9C, the different electronic shells of Mg can be seen, with almost spherical symmetry, very similar to that of the isolated atom, which is indicative of a mainly electrostatic bonding (Zou et al., 2018). In Fig. 9A, the core attractors on the Mg atom are seen to be highly localized. The population of these degenerate attractors was 7.88e, a value well below that expected for 12e Mg, suggesting electron density contribution from the inner shells to the valence regions and strong charge transfer. The V attractor (O_{11}), with a population of 2.34e (slightly higher than the average for this type of attractor (2.30e), is oriented towards the metal and is located at the bond line.

The O_{11}-Mg bond distance was 1.97 A^0, and the total population for V (O_{11}) and V' (O_{11}) was 4.87e; this is a higher value than the average of –OH-type oxygens in the ALG-Mg (4.73e), suggesting that this bond is formed mainly by Mg → O_{11} charge transfer. The electronic localization function diagram shows the Mg-O_{11} interaction, where the binding region presents an ELF value close to zero, which accounts for the electrostatic character of this interaction. The variance value supports the above, which was slightly higher than the average; however, considering the populations, the electronic flux does not vary appreciably, showing that the electronic density is located mainly in the oxygen atom. Meanwhile, the monosynaptic basin V (O_{77}) presents an electronic population of 2.67e, a value higher than the average for this type of attractor (2.58e), and is oriented towards the metal, close to the bond line.

The total population for O_{77} non-bonding attractors was 6.15e, a high value compared to the average (5.34e), indicating a strong charge transfer from Mg to O_{77}. The O_{77}-Mg bond length was 1.84 A^0. The ELF diagram analysis (Fig. 9A and 9B) shows that the interaction region between O_{77} and Mg has an ELF value close to zero, which would indicate a mainly electrostatic binding type. Meanwhile, the value σ^2 is higher than the average value, which suggests an increase in the electronic flux. However, this attractor's population tells us that this increase is very slight, showing that the electron density is located mainly in O_{77}, which allows us to suggest a strong electrostatic interaction between O_{77} and Mg.

Meanwhile, the monosynaptic basin V (O_{12}) is oriented towards the metal but is not located in the O_{12}-Mg bond line. It presents a population of 2.51e, which is above the average value in the system for this type of attractors in ALG-Mg (2.38e). The sum of V (O_{12}) and V' (O_{12}) populations was 5.17e. This value is higher than the average (4.87e). Fig. 9C shows that the interaction region between O_{12} and Mg presents an ELF value close to zero, which indicates a type of electrostatic bond. On the other hand, the variance value is slightly higher than the average value, indicating no significant increase in the electron density flux. However, the short O_{12}-Mg bond distance was 1.97 A^0 (the smallest for O_{12}-metal interactions), indicating that this O_{12}-Mg interaction is the strongest in which O_{12} participates, concerning the other systems under study. Finally, the analysis of the relative fluctuation ($\lambda\left(\bar{N};\Omega_i\right)$) revealed that the electron density tends to be little delocalized; this is consistent with electrostatic bonds between localized negative charges, the oxygens, and the positively charged metal. An important factor to consider is that the absence of 3d electrons would prevent further stabilization by non-bonding electron density delocalization. The basin contribution values of the attractors of the non-bonding pairs of O_{11}, O_{12} and O_{77} were as follows: 97.67% (2.29e) O11 and 2.33% (0.05e) Mg; 98.29% (2.47e) O12 and 1.71% (0.04e);

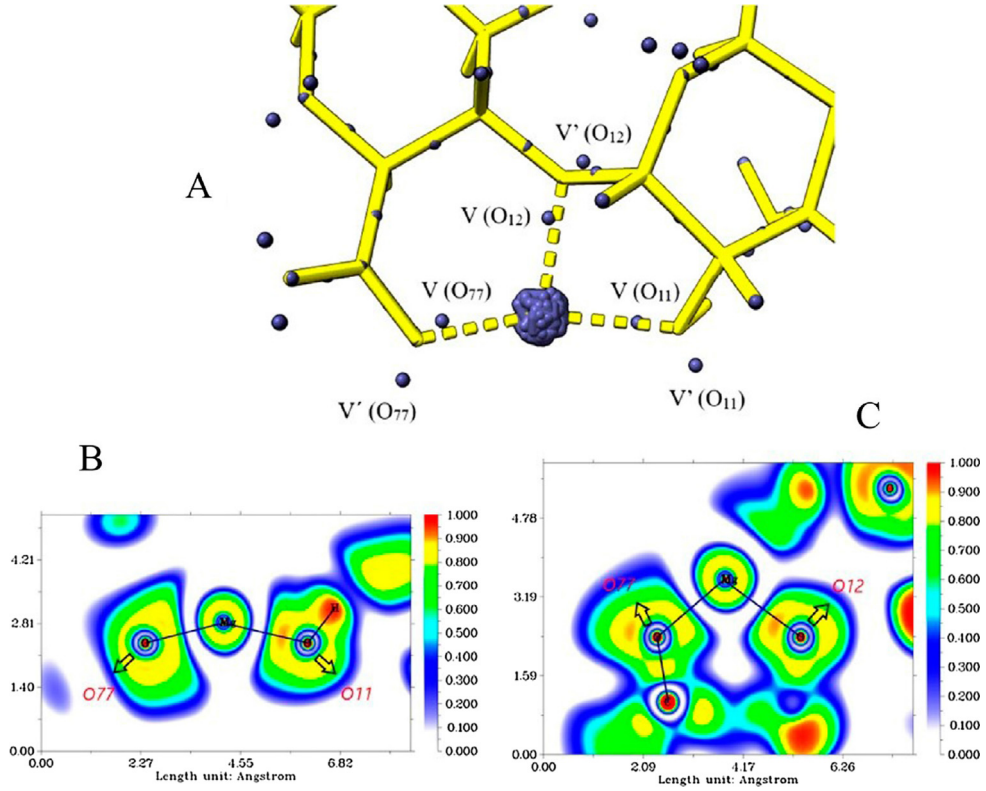

Fig. 9 Attractor populations of the lone pairs of O_{11}, O_{12}, O_{77}, magnesium core, and valence attractors (A). ELF diagrams for the Mg-(O_{77}, O_{11}) interaction (B) and for the Mg-(O_{11}, O_{12}, and O_{77}) interaction (C).

97.15% (2.59e) O77 and 2.85% (0.07e). As can be seen, the metal contributions are low, and the above analyses show that the charge is localized on the oxygens; all this reaffirms the electrostatic description of these bonds (see Table 8).

4.4.4. ALG-Ca

The attractors' populations are presented in Fig. 10A, 10B, and 10C, the ELF diagrams for the ALG-Ca system are shown. In this, the 3 oxygens analyzed are the ones that presented the largest electronic populations (Table 9). The degenerate attractors of the calcium atom core have a population of 15.92e, lower value compared to the expected formal value of 20e. Furthermore, the ELF diagrams (Fig. 10B and 10C) reveal the different electronic layers of the calcium atom, which shows symmetry similar to that of the isolated atom, suggesting a type of electrostatic interaction.

The V (O_{12}) population was 2.45e which is slightly above average for this type of attractors (2.43e), suggesting no $O_{12} \rightarrow Ca$ donation. The total population for the V (O_{12}) and V'(O_{12}) attractors was 5.14e, which is above average (4.89e) for this type of attractors in the ALG-Ca system, suggesting electronic $Ca \rightarrow O_{12}$ donation. The ELF value for the O_{12}-Ca interaction region presents a value close to zero, indicating binding of electrostatic character. Additionally, the high bond distance (3.37 A0) reveals the weakest oxygen-metal interaction of the systems under study. The analysis of σ^2 tells us that the electronic flux increases due to charge transfer from the metal, while the relative flux is slightly higher than the average value (Table 9). The above would confirm the description of a predominantly electrostatic bonding, where the electron density would be located at O12. The V (O_{77}) presented a population of 2.79e, a value higher than the average (2.60e), which indicates electronic transfer $Ca \rightarrow O_{77}$. The sum of both attractors was 6.04e, a value that exceeds the average for attractors of the same type of oxygens (5.41e). The charge transfer would explain this value from the metal to this oxygen

Table 8 Populations (N),variance (σ^2), and relative flux ($\lambda_{(N;\Omega_i)}$), for O_{11}, O_{12}, and O_{77} attractors and average populations ($\bar{N}$), variance ($\bar{\sigma}^2$), and relative flux ($\bar{\lambda}_{(\bar{N};\Omega_i)}$) of other oxygen attractors of: Alcohol, carboxylic acid, and ether, present in ALG-Mg.

Atractor ALG-Mg	*Poblaciones* $\bar{N}/N$ *–OH/, –CO/, -O-*			$\bar{\sigma}^2/\sigma^2$ *–OH/, –CO/, -O-*			$\bar{\lambda}_{(\bar{N};\Omega_i)}/\lambda_{(\bar{N};\Omega_i)}$ *(–OH/, –CO/, -O-)*		
$\bar{V}$(O)	2.30	2.59	2.38	1.12	1.20	1.20	0.48	0.46	0.49
$\bar{V}$(O)	2.43	2.76	2.49	1.13	1.14	1.15	0.46	0.43	0.47
V (O)	**2.34**	**2.67**	**2.51**	**1.15**	**1.27**	**1.23**	**0.49**	**0.48**	**0.49**
V(O)	**2.53**	**3.48**	**2.66**	**1.15**	**1.39**	**1.24**	**0.45**	**0.40**	**0.47**

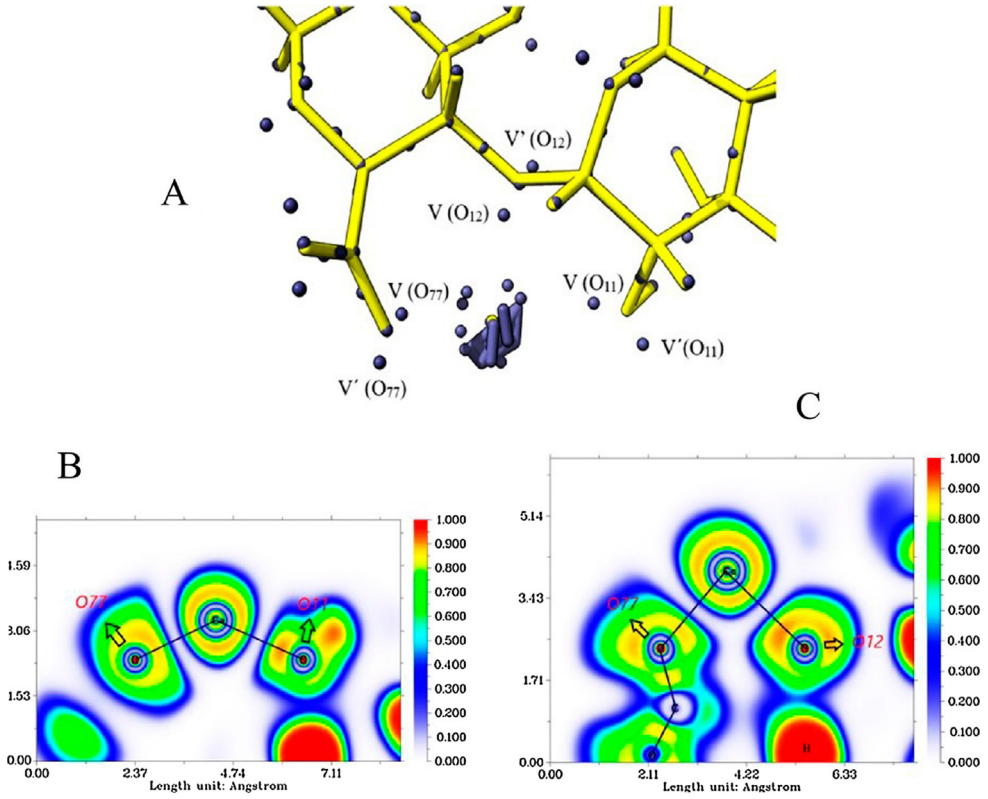

Fig. 10 Attractor populations of the lone pairs of O_{11}, O_{12}, O_{77}, valence, and calcium core attractors (A). ELF diagrams for the Ca-(O_{77}, O_{11}) interaction (B) and for the Ca-(O_{12}, O_{77}) interaction (C).

Table 9 Populations (N), variance (σ^2), and relative flux ($\lambda_{(\bar{N};\Omega_i)}$), for O_{11}, O_{12}, and O_{77} attractors and average populations ($\bar{N}$), variance ($\bar{\sigma}^2$), and relative flux ($\bar{\lambda}_{(\bar{N};\Omega_i)}$) of other oxygen attractors of: Alcohol, carboxylic acid, and ether, present in ALG-Ca.

Attractor ALG-Ca	*Populations* $\bar{N}/N$ *–OH/, –CO/, -O-*			$\bar{\sigma}^2/\sigma^2$ *–OH/, –CO/, -O-*			$\bar{\lambda}_{(\bar{N};\Omega_i)}/\lambda_{(\bar{N};\Omega_i)}$ *(–OH/, –CO/, -O-)*		
$\bar{V}$(O)	2.43	2.60	2.43	1.10	1.20	1.12	0.45	0.46	0.46
$\bar{V}$(O)	2.34	2.81	2.46	1.13	1.18	1.17	0.48	0.42	0.47
V (O)	**2.32**	**2.79**	**2.45**	**1.15**	**1.30**	**1.20**	**0.49**	**0.49**	**0.49**
V(O)	**2.55**	**3.25**	**2.69**	**1.16**	**1.35**	**1.24**	**0.45**	**0.42**	**0.47**

and, as seen in previous systems, by V'(O_{77}) contribution in the π C_{21} = O_{77} bond. The O_{77}-Ca bond distance was 2.52 A0, the highest value obtained for the O_{77} interaction with the different metals. The ELF diagrams suggest a strong electrostatic attraction due to the near-zero value of the electronic localization function. The analysis of variance shows an increase in the electronic flux caused by the charge transfer from the metal, which would suggest a strong electronic delocalization; however, the value of the relative flux indicates that such delocalization is slightly higher than the average values of $\lambda\left(\bar{N};\Omega_i\right)$ for this system, which supports the idea of electrostatic interaction.

The V(O_{11}) attractor had a population of 2.32e, a value lower than the average of 2.43e, suggesting an electronic donation to the metal. Also, the total population for V(O_{11}) and V'(O_{11}) was 4.87e, a value higher than the average for –OH-oxygen attractors (4.77e). The above indicates Ca → O_{11} electron transfer. The analysis of variance and electronic flux shows a situation similar to that of O_{77}, i.e., an increase in electronic flux, in this case, due to donation and *retro*-donation processes, which generate a delocalization only slightly higher than the average values presented in Table 9; this implies a mainly electrostatic bonding. The ELF diagrams Fig. 10B and 10C) also support this electrostatic bonding, which shows the same situation of ELF values close to zero in the interaction region.

Finally, as in ALG-Mg, the oxygen-metal interaction can be represented by negative charges located on the oxygens and positive charges located on the metal. Finally, the contributions to the attractors V (O_{11}), V (O_{12}) and V (O_{77}), were as follows: 98.66% (2.29e) O_{11} and 1.34% (0.05e) Ca; 98.86% (2.42e) O12 and 1.14% (0.02e) Ca; 97.15% (2.59e) O77 and 2.85% (0.04e) Ca. The above is related to the ALG-Mg system's values and supports the electrostatic description of the bonds.

According to the NBO, ELF, and NCI index results, for the different systems under study, the strongest interaction with O_{77} follows the following order: Cu ≅Mn > Mg > Ca, where Mn and Cu present polar covalent bonding, while Ca and Mg electrostatic bonds. For O_{11}: Cu ≅Mn ≫ Mg > Ca, where Mn and Cu present polar covalent bonds, while Ca and Mg electrostatic bonds and for O_{12}: Mg > Cu ≅Ca ≫ Mn, all these interactions are electrostatic. Finally, these results correlate with the analysis of the overall reactivity indices. According to our results, the stability order is as follows: ALG-Cu > ALG-Mn > ALG-Mg > ALG-Ca.

Our results contradict some previous studies regarding the type of interactions between alginate and divalent cations. It has been mentioned, for example, that cations such as Mn^{2+} would bind weakly to the polymer, mainly by electrostatic interactions (Emmerichs et al., 2004). It has also been reported that Mg^{2+} binds more weakly than calcium because the former shows little or no tendency to form hydrogels (Topuz et al., 2012). Furthermore, as already mentioned, other studies indicate that the degree of affinity is not correlated with the bond's strength (see Refs. 12 and 13), whose results, concerning the type of interactions, agree with those presented in this work. Finally, our study supports the idea of the lack of correlation between bond strength and affinity.

5. Conclusions

The overall reactivity indices showed higher stability for the systems under study, given the following order: ALG-Cu > ALG-Mn > ALG-Mg > ALG-Ca, which seems to be correlated with the degree of electronic delocalization and the degree of covalency of the bonds. As for the nature of the bonds in the ALG-Cu and ALG-Mn systems, these were between the carboxylic acid and alcohol groups' oxygens and proved to be of polar covalent, whereas with the ether oxygen, it is predominantly electrostatic. For the latter, Mn presented a weak interaction, and Mg the strongest. Whereas, in ALG-Ca and ALG-Mg, all the oxygen-metal bonds studied were of electrostatic nature.

Declaration of Competing Interest

The authors declare that they have no known competing financial interests or personal relationships that could have appeared to influence the work reported in this paper.

Acknowledgements

The authors would like to thank Dr. María Camarada, Director of the Center for Applied Nanotechnology, Faculty of Sciences Universidad Mayor, for providing the means to carry out this study. Cristian Castro thanks the regular FONDECYT project 1130676.

References

Agulhon, P., Markova, V., Robitzer, M., Quignard, F.O., Mineva, T., 2012. Structure of alginate gels: interaction of diuronate units with divalent cations from density functional calculations. Biomacromolecules 13, 1899–1907. https://doi.org/10.1021/bm300420z.

Bekri, L., Zouaoui-Rabah, M., Springborg, M., & Rahal, M.S.J.J.o.m.m., 2018. A structural DFT study of MM, GG, MG, and GM alginic acid disaccharides and reactivity of the MG metallic complexes, Journal of molecular modeling, 24, 1-13.

Bidarra, S.J., Barrias, C.C., Granja, P.L., 2014. Injectable alginate hydrogels for cell delivery in tissue engineering. Acta Biomater. 10, 1646–1662. https://doi.org/10.1016/j.actbio.2013.12.006.

Boto, R.A., Peccati, F., Laplaza, R., Quan, C., Carbone, A., Piquemal, J.-P., Maday, Y., Contreras-García, J., 2020. NCIPLOT4: Fast, Robust, and Quantitative Analysis of Noncovalent Interactions. J. Chem. Theory Comput. 16, 4150–4158. https://doi.org/10.1021/acs.jctc.0c00063.

Bouhadir, K.H., Kruger, G.M., Lee, K.Y., Mooney, D.J., 2000. Sustained and controlled release of daunomycin from cross-linked poly (aldehyde guluronate) hydrogels. J. Pharm. Sci. 89, 910–919. https://doi.org/10.1002/1520-6017(200007)89:7<910::AID-JPS8>3.0.CO;2-#.

Chan, L., Jin, Y., Heng, P., 2002. Cross-linking mechanisms of calcium and zinc in production of alginate microspheres. Int. J. Pharm. 242, 255–258. https://doi.org/10.1016/S0378-5173(02)00169-2.

Chandrasekaran, K., Kumar, R.T., 2015. Structural, spectral, thermodynamical, NLO, HOMO, LUMO and NBO analysis of fluconazole. Spectrochim. Acta Part A Mol. Biomol. Spectrosc. 150, 974–991. https://doi.org/10.1016/j.saa.2015.06.018.

Chattaraj, P.K., Giri, S., 2009. Electrophilicity index within a conceptual DFT framework. Ann. Rep. Sect. C (Physical Chemistry) 105, 13–39. https://doi.org/10.1039/B802832J.

Chaudret, R., Piquemal, J.-P., Cisneros, G.A., 2011. Correlation between electron localization and metal ion mutagenicity in DNA synthesis from QM/MM calculations. PCCP 13, 11239–11247. https://doi.org/10.1039/C0CP02550J.

Chauvin, R., Lepetit, C., Silvi, B., Alikhani, E., 2016. Applications of Topological Methods in Molecular Chemistry Vol. 22, 1–586.

Chen, Y., Teng, J., Liao, B.-Q., Li, R., Lin, H., 2020. Molecular insights into the impacts of iron (III) ions on membrane fouling by alginate. Chemosphere 242,. https://doi.org/10.1016/j.chemosphere.2019.125232 125232.

Contreras-García, J., Boto, R.A., Izquierdo-Ruiz, F., Reva, I., Woller, T., Alonso, M., 2016. A benchmark for the non-covalent interaction (NCI) index or... is it really all in the geometry? Theor. Chem. Acc. 135, 1–14. https://doi.org/10.1007/s00214-016-1977-7.

Durlak, P., Latajka, Z., Berski, S., 2009. A Car-Parrinello and path integral molecular dynamics study of the intramolecular lithium bond in the lithium 2-pyridyl-N-oxide acetate. J. Chem. Phys. 131,. https://doi.org/10.1063/1.3175797 024308.

Emmerichs, N., Wingender, J., Flemming, H.-C., Mayer, C., 2004. Interaction between alginates and manganese cations: identification of preferred cation binding sites. Int. J. Biol. Macromol. 34, 73–79. https://doi.org/10.1016/j.ijbiomac.2004.03.004.

Fekri, M.H., Bazvand, R., Soleymani, M., Razavi Mehr, M., 2020. Adsorption of Metronidazole drug on the surface of nano fullerene C60 doped with Si, B and Al: A DFT study. Int. J. Nano Dimens. 11, 346–354.

Filipiuk, D., Fuks, L., Majdan, M., 2005. Transition metal complexes with uronic acids. J. Mol. Struct. 744, 705–709. https://doi.org/10.1016/j.molstruc.2004.11.073.

Fuentealba, P., Chamorro, E., Santos, J.C., 2007. Understanding and using the electron localization function. Theor. Comput. Chem. 19, 57–85. https://doi.org/10.1016/S1380-7323(07)80006-9.

Fuster, F., Dézarnaud-Dandine, C., Chevreau, H., Sevin, A., 2004. A theoretical study of the bonding in NO,(NO) 2,(NO) 2− and (NO) 2 2− using a topological analysis of the electron localization function. PCCP 6, 3228–3234. https://doi.org/10.1039/B401310G.

Grant, G.T., Morris, E.R., Rees, D.A., Smith, P.J., Thom, D., 1973. Biological interactions between polysaccharides and divalent cations: the egg-box model. FEBS Lett. 32, 195–198. https://doi.org/10.1016/0014-5793(73)80770-7.

Hasan, I., Khan, R.A., Alharbi, W., Alharbi, K.H., Khanjer, M.A., Alslame, A., 2020a. Synthesis, characterization and photo-catalytic activity of guar-gum-g-aliginate@ silver bionanocomposite material. RSC Adv. 10, 7898–7911. https://doi.org/10.1039/D0RA00163E.

Hasan, I., Shekhar, C., Alharbi, W., Abu Khanjer, M., Khan, R.A., Alsalme, A., 2020b. A highly efficient Ag nanoparticle-immobilized alginate-g-polyacrylonitrile hybrid photocatalyst for the degradation of nitrophenols. Polymers 12, 3049. https://doi.org/10.3390/polym12123049.

Hasan, I., Shekhar, C., Bin Sharfan, I.I., Khan, R.A., Alsalme, A., 2020c. Ecofriendly Green Synthesis of the ZnO-Doped CuO@ Alg Bionanocomposite for Efficient Oxidative Degradation of p-Nitrophenol. ACS Omega 5, 32011–32022. https://doi.org/10.1021/acsomega.0c04917.

Haug, A., 1961. Affinity of some divalent metals to different types of alginates. Acta Chem. Scand. 15, 1794–2000.

Henkel, J., Woodruff, M.A., Epari, D.R., Steck, R., Glatt, V., Dickinson, I.C., Choong, P.F., Schuetz, M.A., Hutmacher, D.W., 2013. Bone regeneration based on tissue engineering conceptions—a 21st century perspective. Bone Res. 1, 216–248. https://doi.org/10.4248/BR201303002.

Jerabek, P., Schuetrumpf, B., Schwerdtfeger, P., Nazarewicz, W., 2018. Electron and Nucleon Localization Functions in Superheavy Elements. Phys. Rev. Lett 120,. https://doi.org/10.1103/PhysRevLett.120.053001 053001.

Kohn, R., 1975. Ion Binding On Polyuronats—Alginate Pectin. In: Khalaf, Moayad N. (Eds.) Green Polymers and Environmental Pollution Control, Apple Academic Press Inc, pp. 239–263.

Lee, L.P., Cole, D.J., Payne, M.C., Skylaris, C.K., 2013. Natural bond orbital analysis in the ONETEP code: applications to large protein systems. J. Comput. Chem. 34, 429–444. https://doi.org/10.1002/jcc.23150.

Lefebvre, C., Rubez, G., Khartabil, H., Boisson, J.-C., Contreras-García, J., Hénon, E., 2017. Accurately extracting the signature of intermolecular interactions present in the NCI plot of the reduced density gradient versus electron density. PCCP 19, 17928–17936. https://doi.org/10.1016/j.jhazmat.2020.123815.

Li, L., Fang, Y., Vreeker, R., Appelqvist, I., Mendes, E., 2007. Reexamining the egg-box model in calcium− alginate gels with X-ray diffraction. Biomacromolecules 8, 464–468. https://doi.org/10.1021/bm060550a.

Lin, X., Wu, W., Mo, Y., 2020. A theoretical perspective of the agostic effect in early transition metal compounds. Coord. Chem. Rev. 419,. https://doi.org/10.1016/j.ccr.2020.213401 213401.

Liu, S., Rong, C., Lu, T., Hu, H., 2018. Identifying strong covalent interactions with Pauli energy. J. Phys. Chem. A 122, 3087–3095. https://doi.org/10.1021/acs.jpca.8b00521.

Lu, L., Liu, X., Dai, L., Tong, Z., 2005. Difference in concentration dependence of relaxation critical exponent n for alginate solutions at sol− gel transition induced by calcium cations. Biomacromolecules 6, 2150–2156. https://doi.org/10.1021/bm050126u.

Lu, X., Duchimaza-Heredia, J., Cui, Q., 2019. Analysis of Density Functional Tight Binding with Natural Bonding Orbitals. J. Phys. Chem. A 123, 7439–7453. https://doi.org/10.1021/acs.jpca.9b05072.

Mierzwa, G., Gordon, A.J., Berski, S., 2020. The nature of the triple BB, double, BB, single, B-B, and one-electron, BB boron-boron bonds from the topological analysis of electron localisation function (ELF) perspective. J. Mol. Struct. 1221,. https://doi.org/10.1016/j.molstruc.2020.128530 128530.

Mierzwa, G., Gordon, A.J., Berski, S., 2018. On the nature of the boron–copper interaction. Topological study of the electron localisation function (ELF). New J. Chem. 42, 17096–17114. https://doi.org/10.1039/C8NJ03516D.

Mørch, Y.A., Qi, M., Gundersen, P.O.M., Formo, K., Lacik, I., Skjåk-Bræk, G., Oberholzer, J., Strand, B.L., 2012. Binding and leakage of barium in alginate microbeads. J. Biomed. Mater. Res. Part A 100, 2939–2947. https://doi.org/10.1002/jbm.a.34237.

Obot, I., Macdonald, D., Gasem, Z., 2015. Density functional theory (DFT) as a powerful tool for designing new organic corrosion inhibitors. Part 1: an overview. Corros. Sci. 99, 1–30. https://doi.org/10.1016/j.corsci.2015.01.037.

Papageorgiou, S.K., Kouvelos, E.P., Favvas, E.P., Sapalidis, A.A., Romanos, G.E., Katsaros, F.K., 2010. Metal–carboxylate interactions in metal–alginate complexes studied with FTIR spectroscopy. Carbohydr. Res. 345, 469–473. https://doi.org/10.1016/j.carres.2009.12.010.

Pearson, R.G., 1993. The principle of maximum hardness. Acc. Chem. Res. 26, 250–255. https://doi.org/10.1021/ar00029a004.

Pilmé, J., 2017. Electron localization function from density components. J. Comput. Chem. 38, 204–210. https://doi.org/10.1002/jcc.24672.

Platts, J.A., Baker, R.J., 2020. A computational investigation of orbital overlap versus energy degeneracy covalency in [UE 2] 2 +(E= O, S, Se, Te) complexes. Dalton Trans. 49, 1077–1088. https://doi.org/10.1039/C9DT04484A.

Poater, J., Duran, M., Sola, M., Silvi, B., 2005. Theoretical evaluation of electron delocalization in aromatic molecules by means of atoms in molecules (AIM) and electron localization function (ELF) topological approaches. Chem. Rev. 105, 3911–3947. https://doi.org/10.1021/cr030085x.

Raju, S., Singh, H.B., Butcher, R.J., 2020. Metallophilic interactions: observations of the shortest metallophilicinteractions between closed shell (d 10⋯ d 10, d 10⋯ d 8, d 8⋯ d 8) metal ions [M⋯ M′ M= Hg (ii) and Pd (ii) and M′= Cu (i), Ag (i), Au (i), and Pd (ii)]. Dalton Trans. 49, 9099–9117. https://doi.org/10.1039/D0DT01008A.

Raub, S., Jansen, G., 2001. A quantitative measure of bond polarity from the electron localization function and the theory of atoms in molecules. Theor. Chem. Acc. 106, 223–232. https://doi.org/10.1007/s002140100268.

Savin, A., Nesper, R., Wengert, S., Fässler, T.F., 1997. ELF: The electron localization function. Angew. Chem., Int. Ed. Engl. 36, 1808–1832. https://doi.org/10.1002/anie.199718081.

Savin, A., Silvi, B., Colonna, F., 1996. Topological analysis of the electron localization function applied to delocalized bonds. Can. J. Chem. 74, 1088–1096. https://doi.org/10.1139/v96-122.

Topuz, F., Henke, A., Richtering, W., Groll, J., 2012. Magnesium ions and alginate do form hydrogels: a rheological study. Soft Matter 8, 4877–4881. https://doi.org/10.1039/C2SM07465F.

Wang, B., Wan, Y., Zheng, Y., Lee, X., Liu, T., Yu, Z., Huang, J., Ok, Y.S., Chen, J., Gao, B., 2019. Alginate-based composites for environmental applications: a critical review. Crit. Rev. Environ. Sci. Technol. 49, 318–356. https://doi.org/10.1080/10643389.2018.1547621.

Weinhold, F., Landis, C., Glendening, E., 2016. What is NBO analysis and how is it useful? Int. Rev. Phys. Chem. 35, 399–440. https://doi.org/10.1080/0144235X.2016.1192262.

Xu, Z., Lam, M.T., 2018. Alginate application for heart and cardiovascular diseases. In: Alginates and Their Biomedical Applications, Springer, pp. 185–212. https://doi.org/10.1007/978-981-10-6910-9.

Yang, Y., Weaver, M.N., & Merz Jr, K.M.J.T.J.o.P.C.A. (2009). Assessment of the "6-31+ G**+ LANL2DZ" mixed basis set coupled with density functional theory methods and the effective core potential: prediction of heats of formation and ionization potentials for first-row-transition-metal complexes. The Journal of Physical Chemistry A, 113(36), 9843-9851.

Zhao, D.-X., Zhao, J., Yang, Z.-Z., 2020. Partitioning a Molecule into the Atomic Basins and the Resultant Atomic Charges from Quantum Chemical Topology Analysis of the Kohn-Sham Poten-

tial. J. Phys. Chem. A 124, 5023–5032. https://doi.org/10.1021/acs.jpca.0c01289.

Zou, G., Jo, H., Lim, S.J., You, T.S., Ok, K.M., 2018. Rb3VO (O2) 2CO3: A Four-in-One Carbonatoperoxovanadate Exhibiting an Extremely Strong Second-Harmonic Generation Response. Angew. Chem. Int. Ed. 57, 8619–8622. https://doi.org/10.1002/anie.201804354.

Zülfikaroğlu, A., Batı, H., Dege, N., 2018. A theoretical and experimental study on isonitrosoacetophenone nicotinoyl hydrazone: Crystal structure, spectroscopic properties, NBO, NPA and NLMO analyses and the investigation of interaction with some transition metals. J. Mol. Struct. 1162, 125–139. https://doi.org/10.1016/j.molstruc.2018.02.079.